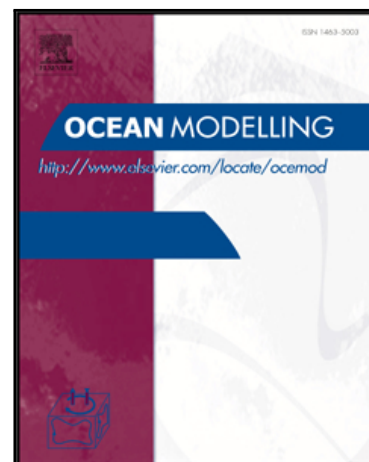


## Accepted Manuscript

Mesoscale mixing of the Denmark Strait Overflow in the Irminger Basin

Inga. M. Koszalka, Thomas W.N. Haine, Marcello G. Magaldi

PII: S1463-5003(17)30026-4  
DOI: [10.1016/j.ocemod.2017.03.001](https://doi.org/10.1016/j.ocemod.2017.03.001)  
Reference: OCEMOD 1180



To appear in: *Ocean Modelling*

Received date: 2 August 2016  
Revised date: 24 February 2017  
Accepted date: 2 March 2017

Please cite this article as: Inga. M. Koszalka, Thomas W.N. Haine, Marcello G. Magaldi, Mesoscale mixing of the Denmark Strait Overflow in the Irminger Basin, *Ocean Modelling* (2017), doi: [10.1016/j.ocemod.2017.03.001](https://doi.org/10.1016/j.ocemod.2017.03.001)

This is a PDF file of an unedited manuscript that has been accepted for publication. As a service to our customers we are providing this early version of the manuscript. The manuscript will undergo copyediting, typesetting, and review of the resulting proof before it is published in its final form. Please note that during the production process errors may be discovered which could affect the content, and all legal disclaimers that apply to the journal pertain.

## 1 **Highlights**

- 2     • Water mass transformation in Denmark Strait Overflow is localized in  
3       space/time
- 4     • High transformation co-locates with maxima in eddy velocity variance  
5       and shear
- 6     • Overflow eddies modulate the transformation, eddy heat flux diver-  
7       gence and shear

# Mesoscale mixing of the Denmark Strait Overflow in the Irminger Basin

Inga. M . Koszalka<sup>a,b,\*</sup>, Thomas W. N. Haine<sup>b</sup>, Marcello G. Magaldi<sup>a,b</sup>

<sup>a</sup>*GEOMAR–Helmholtz Centre for Ocean Research Kiel, Duesternbrooker Weg 20, 24105 Kiel, Germany*

<sup>b</sup>*Johns Hopkins University, Earth and Planetary Sciences, Baltimore, USA*

<sup>c</sup>*CNR–Consiglio Nazionale delle Ricerche, ISMAR–Istituto di Scienze Marine, Lerici, Italy*

## Abstract

The Denmark Strait Overflow (DSO) is a major export route for dense waters from the Nordic Seas forming the lower limb of the Atlantic Meridional Overturning Circulation, an important element of the climate system. Mixing processes along the DSO pathway influence its volume transport and properties contributing to the variability of the deep overturning circulation. They are poorly sampled by observations however which hinders development of a proper DSO representation in global circulation models. We employ a high resolution regional ocean model of the Irminger Basin to quantify impact of the mesoscale flows on DSO mixing focusing on geographical localization and local time–modulation of water property changes. The model reproduces the observed bulk warming of the DSO plume 100–200 km downstream of the Denmark Strait sill. It also reveals that mesoscale variability of the overflow (‘DSO-eddies’, of 20–30 km extent and a time scale of 2–5 day) modulates water property changes and turbulent mixing, diagnosed with the vertical shear of horizontal velocity and the eddy heat flux divergence. The space–time localization of the DSO mixing and warming and the role of coherent mesoscale structures should be explored by turbulence measurements and factored into the coarse circulation models.

## Keywords:

Denmark Strait Overflow, mesoscale, mixing, vertical eddy heat flux, internal waves

\*Corresponding author

Email address: [ikoszalka@geomar.de](mailto:ikoszalka@geomar.de) (Inga. M . Koszalka)

## 1. Introduction

The Denmark Strait Overflow (DSO) Water (potential density referenced to the surface  $\sigma_\theta = \rho_\theta - 1000 \geq 27.8 \text{ kg m}^{-3}$ , the units are dropped hereafter) is a mixture of water masses formed in the Arctic and the Nordic Seas. At the Denmark Strait (DS) sill the DSO appears as a hydraulically controlled flow (Whitehead, 1998; Käse and Oschlies, 2000; Girton *et al.*, 2001; Macrander *et al.*, 2005; Dickson *et al.*, 2008; Jungclauss *et al.*, 2008) with a mean volume flux of approximately 3.4 Sv and variance of 2 Sv<sup>2</sup> (**1 Sv =  $10^6 \text{ m}^3 \text{ s}^{-1}$** ), and showing **no detectable trend in the time series over the 15-year observation period** (1996–2011 Jochumsen *et al.*, 2012). The highest variability in the volume flux is associated with pulses with time scales of 2–10 days (1.5 Sv<sup>2</sup> variance in the mooring time series) and attributed to the mesoscale features. Seasonal variability is weak and explains less than 5%, and the interannual variability is on the order of 10% of the mean (Jochumsen *et al.*, 2012). Modeling studies associate the interannual variability of the DSO volume flux to the wind forcing (Köhl *et al.*, 2007) though this relation is not clear in the mooring observations (Jochumsen *et al.*, 2012). At the DS sill, also the DSO water composition (temperature, salinity) exhibits interannual-to-decadal variations due to changes in the upstream source waters or pathways (Rudels *et al.*, 2003; Serra *et al.*, 2010).

Leaving the sill, the DSO is composed of mesoscale (20–30 km) boluses of dense water cascading into the Irminger Basin at intervals of 2–5 days (e.g., Girton and Sanford, 2003; Magaldi *et al.*, 2011) with a smaller contribution (estimated 0.5–1 Sv) of dense waters recirculating on the shelf and spilling off into the basin downstream off the sill (e.g., Pickart *et al.*, 2005; Koszalka *et al.*, 2013; Jochumsen *et al.*, 2015). **The boluses are overlaid by cyclonic eddies documented by observations (Bruce, 1995; von Appen *et al.*, 2014b) and regional models (e.g., Käse *et al.*, 2003; Magaldi *et al.*, 2011; Magaldi and Haine, 2014). These cyclonic eddies formed either through stretching of the water during the descent of boluses from the sill (Bruce, 1995; von Appen *et al.*, 2014b), or through friction effects (Hill, 1996), or a combination of both mechanisms (Käse *et al.*, 2003). Downstream at the SJ section, the bolus-eddy structures propagating with speeds of  $\sim 0.5 \text{ m/s}$  and extending over the entire water column are seen in observations (von Appen *et al.*, 2014b) and models (e.g., Magaldi *et al.*, 2011; Magaldi and Haine, 2014). In the Irminger Basin the**

DSO follows the continental slope of the East Greenland Shelf toward the North Atlantic where it supplies about one third of the North Atlantic Deep Water, a major component of the Atlantic Meridional Overturning Circulation (AMOC, Dickson *et al.*, 2008). The DSO contributes to the AMOC also indirectly through its impact on stratification and thus on convection in the Labrador Sea. For these reasons, quantifying and understanding DSO variability and its adequate parameterization in global circulation models (GCMs) is of high priority (Legg *et al.*, 2009; Yeager and Danabasoglu, 2012; Danabasoglu and Coauthors, 2014; Wang *et al.*, 2015; Guo *et al.*, 2016).

During its transit through the Irminger Basin, the DSO is subject to mixing processes that cause entrainment of ambient waters and transformation of the overflow in terms of water mass properties. Thus, the water properties of the DSO in the North Atlantic depend on both changes in the source waters north of the DS sill and mixing processes in the Irminger Basin. While the variability at the DS sill is relatively well quantified and monitored (Jochumsen *et al.*, 2012), the mixing processes downstream remain obscure due to the scarcity of direct observations. The present study aims to elucidate downstream mixing and guide future measurements by using a high resolution model.

The spatial distribution of entrainment and water mass property transformation in the DSO have been indirectly estimated from observations. Between the DS sill and the Spill Jet (SJ) section, 285 km southwest, the DSO nearly doubles its volume flux (to  $\sim 5.2$  Sv, Brearley *et al.*, 2012) and decreases its density by over  $0.1 \text{ kg m}^{-3}$  (Girton and Sanford, 2003). Oxygen measurements at the SJ section suggest that some of the DSO water has transformed into intermediate waters ( $\sigma_\theta < 27.8$ ; Brearley *et al.*, 2012), consistent with forward and backward Lagrangian simulations (Koszalka *et al.*, 2013; von Appen *et al.*, 2014a). The detrainment implies that the entrainment must be higher than calculated from the increase in DSO transport alone.

Further downstream the entrainment rate drops: at the Angmagssalik line, 530 km from the sill, the measured DSO transport is 6 Sv (Dickson *et al.*, 2008). Thus, the majority of DSO transformation appears to occur in a  $\sim 300$  km region between DS and the SJ section, corresponding to only a few grid cells of a typical GCM. In lieu of direct turbulence observations, Voet and Quadfasel (2010, hereafter VQ2010) used moored temperature and velocity timeseries collected in years 1999–2005 at four sections along the DSO pathway. They found the highest warming rate ( $\sim 500 \text{ mK/100 km}$ )

between the DS sill and the next section 200 km downstream and an order of magnitude smaller warming rate further downstream. Based on budget calculations, VQ2010 deduced that the vertical mixing is responsible for strong DSO warming near the sill while the term attributable to the mesoscale variability ('horizontal eddy stirring') is strong enough to account for the low warming rates further downstream. The hostility of the environment and high DSO speeds make turbulence measurements hard and only a few microstructure (turbulent fluctuation intensity in temperature and velocity) profiles downstream of the sill exist (Paka *et al.*, 2013; Schaffer *et al.*, 2016). The latter work presents recent turbulence observations from autonomous vehicles deployed 180 km from the sill. Their results highlight a transient nature of mixing processes and suggest that both horizontal advection of warm water and vertical mixing of it into the plume are eddy-driven and are important in the region, as is the interaction of the overflow with topography. Thus a quantitative observational assessment of the mixing processes contributing to the intense DSO water mass property and volume flux changes near the sill remains elusive.

In this work, we use a high resolution numerical model to diagnose the local impact of mesoscale variability on the DSO mixing and water mass property changes in view of motivating future work on DSO mixing parameterizations in coarse resolution models that would properly represent it. The paper is organized as follows. Section 2 describe the regional ocean model as well as the Lagrangian particle model used in the study. Section 3 presents the results focusing on two aspects: localization of overflow water property changes, vertical mixing diagnostics and mesoscale energy in geographical space (a 100-km region along the overflow path close to the Denmark Strait, Sect. 3.1–3.2) and time-modulation of the vertical property eddy fluxes by mesoscale variability locally (Sect. 3.3). Section 4 discusses the results and concludes the paper.

## 2. Methods

A hydrostatic version of the Massachusetts Institute of Technology general circulation model (MITgcm) is used. The configuration is described in Koszalka *et al.* (2013): it features a horizontal grid spacing of 2 km and 210 levels in the vertical (grid cell height of 15 m below 100 m), which makes our model a highest-to-date resolution regional ocean model of the Irminger Basin. There are three open boundaries; the western boundary is closed at

the east coast of Greenland. The simulation spans the summer of 2003 (1 July–1 September). The boundary conditions are obtained from the 1/128-resolution North Atlantic experiment of the Hybrid Coordinate Ocean Model (Chassignet and Coauthors, 2009). No-slip conditions are applied to all material boundaries. For the wind stress, we use the composite SeaWinds product (Zhang *et al.*, 2006). Other atmospheric forcing variables are derived from the National Centers for Environmental Prediction reanalysis (Kalnay and Coauthors, 1996). The tides are excluded in our configuration as they are weak in this area (von Appen *et al.*, 2014b, VQ2010).

The model uses partial bottom cells and a rescaled height coordinate (Adcroft and Campin, 2004) to accurately simulate the dense current flowing against the continental slope in the Irminger Basin. It also features a non-linear free surface, a flow-dependent Leith biharmonic viscosity and a third-order advection scheme with zero explicit horizontal diffusivity for tracers. A non-local K-Profile Parametrization (KPP) scheme (Large *et al.*, 1994) is used to parametrize unresolved vertical mixing processes. The scheme employs Monin-Obukhov similarity theory to compute the surface boundary layer depth and vertical mixing rate as a function of surface fluxes. Below the surface boundary layer, the scheme sums contributions due to internal wave breaking (represented by a constant background viscosity,  $\nu^o = 10^{-5} \text{ m}^2 \text{ s}^{-1}$ ), as well as shear instability, and convective mixing as functions of the local Richardson number  $Ri = N^2/Sh^2$ , where  $N$  is the local buoyancy frequency and measures the stratification, and the resolved squared horizontal velocity  $(u, v)$  shear is  $Sh^2 = (\partial_z u)^2 + (\partial_z v)^2$ . For the mixing rate due to shear instability,  $\nu^s$ , we have:

$$\begin{aligned} \nu^s/\nu^o &= [1 - (Ri/Ri_o)^2]^3 & 0 < Ri < Ri_o \\ \nu^s/\nu^o &= 1 & Ri > Ri_o, \end{aligned} \quad (1)$$

where  $Ri_o = 0.7$ . The convective mixing ( $N^2, Ri < 0$ ) is parameterized implicitly with  $\nu_c = 0.015 \text{ m}^2 \text{ s}^{-1}$ . The model diagnostics rely on a 15-minute storage period for model fields.

The simulation has been compared to observations of dense and intermediate water volume fluxes as well as the hydrography at standard sections, with very good agreement (Magaldi *et al.*, 2011; Koszalka *et al.*, 2013).

To map the DSO pathway along the slope and its transformation we employ a set of  $\mathcal{O}(10,000)$  Lagrangian particles released at the Denmark

164 Strait and simulated offline using model three-dimensional velocity fields as  
 165 described in Koszalka *et al.* (2013). The particles were released in dense  
 166 waters ( $\sigma_\theta \geq 27.8$ ) along a section intercepting the Denmark Strait sill and  
 167 the adjacent shelf, separated by 2 km in the horizontal and 25 m in vertical.  
 168 The particles were released ten times every 12 hours over a five day period (1–  
 169 5 July 2003) encompassing a passage of a mesoscale bolus and a silent period  
 170 between the boluses. The majority of particles deployed at the sill followed  
 171 the continental slope in the Irminger Basin crossing the Angmagssalik line  
 172 within 3 weeks; those deployed on the shelf recirculate on the Dohrn Bank  
 173 and around the Kangerdlugssuaq Trough spilling off the Irminger Basin at  
 174 various locations along the shelf break. The ensemble-mean positions of  
 175 particles and the ensemble particle density transformation agrees well with  
 176 available observations of the DSO (Koszalka *et al.*, 2013).

### 177 3. Results

178 In this study, we only consider simulated particles that at a given time  
 179 instant satisfy: (1) the dense-water ( $\sigma_\theta \geq 27.8$ ) condition and, (2) are located  
 180 on the continental slope below the shelf break (marked by the 450 m isobath),  
 181 i.e., the particles following the ‘traditional’ DSO pathway along the conti-  
 182 nental slope (e.g., Dickson *et al.*, 2008, VQ2010). This selection excludes  
 183 the dense water pathways on the shelf but includes dense waters that spilled  
 184 off the shelf downstream of the Denmark Strait and follow the slope there-  
 185 after. A sequence of particle positions obeying these conditions, projected  
 186 on a horizontal plane, is shown in Figure 1.

#### 187 3.1. The DSO velocity and water mass transformation along its pathway

188 The DSO pathway in the Irminger Basin traced by the time- and depth-  
 189 averaged particle positions is marked with yellow dots in fig. 2a. Time-  
 190 averaged (Eulerian) vertical profiles of the along-stream velocity from key  
 191 stations along this pathway show the average evolution of the DSO as a  
 192 part of the boundary current (fig. 2b). The bottom-intensified dense plume  
 193 accelerates during the initial descent from the sill. Passing along the slope  
 194 below the Dohrn Bank and at the TTO section (stations s3–4), the DSO  
 195 exhibits highest velocities ( $\sim 1$  m/s) with a pronounced ‘nose’ above a bot-  
 196 tom boundary layer. After descending into the Irminger Basin, the DSO  
 197 slows down to 0.25–0.35 m/s by the Sermilik Deep Opening (SDO, s6) and



the Angmagssalik section (s7), consistent with observations (Dickson *et al.*, 2008).

To quantify the model DSO warming along its pathway, we calculate the mean Lagrangian DSO warming rate as function of distance from the DS sill derived from the particle temperatures averaged in 20km-distance bins starting at the DS sill (-27.1°W, 66.1°N). The bins have no off-shore boundary encompassing all particles thus their lateral span varies depending on local particle distribution (about 50 km at the sill and up to 200 km downstream, see fig. 1). Each bin contains at least 1000 particles. The mean Lagrangian DSO warming rate derived from binning (fig. 2c) is consistent with six-year means of VQ2010 estimated from the hydrographic sections. The model DSO warming rate, however, exhibits a complicated spatial structure with a maximum (500–2000 mK/100 km) localized near stations 3–4 (120–180 km from the sill) where the DSO speed is fastest (fig. 2b). Downstream of the SJ section, the DSO warming rates drop rapidly and then fluctuate about zero ( $\pm 100$  mK/100km; VQ2010 report  $\pm 50$  mK/100km). These results correspond to a mean DSO warming by 1–1.5 K over the initial 200 km, between the DS sill and the TTO section, and little temperature transformation further downstream in agreement with the observational study of VQ2010. Note that these results differ slightly from Koszalka *et al.* (2013, their fig. 6b): their region of high transformation extended to the shelf break and shelf because it also included particles recirculating on the shelf.

We also include the Eulerian estimate of the warming rate in figure 2c (light green), derived from timeseries at the model grid points satisfying the DSO conditions. The Eulerian DSO warming rate is higher than the Lagrangian estimate in the first 100 km from the sill. This is because the Lagrangian estimate is conditioned on the particle deployment site. The Eulerian estimate derived from averaging in the grid points, on the other hand, include dense waters recirculating in the sill vicinity which are more likely to have been mixing with warm waters of the Irminger current flowing into the Denmark Strait (Magaldi *et al.*, 2011; Jochumsen *et al.*, 2015).

Figure 2d shows a scatterplot of the mean warming and buoyancy gain rates along the DSO path. Both, Lagrangian and Eulerian estimates suggest a linear relationship supporting the choice of the temperature as a proxy for the density changes in the overflow plume as proposed by VQ2010.

### 3.2. Spatially localized mixing and mesoscale variability

Here we investigate Eulerian time-mean diagnostics relevant to the DSO mixing and warming along its pathway in the Irminger Basin. Figure 3a shows a time-mean vertical shear of horizontal velocity resolved by the model,  $Sh$ , a key variable in many mixing parameterizations (Large *et al.*, 1994; Legg *et al.*, 2009). The shear is high in the bottom  $\sim 100$  m along the entire pathway, but the maximum occurs at s3 (DB) where the high shear extends over the entire water column. The inverse Richardson number,  $Ri^{-1} = Sh^2/N^2$  is  $\mathcal{O}(100)$  suggesting the importance of shear-driven turbulence in mixing and the attendant DSO warming that peaks in this area (fig. 2c). The intensified mixing and shear co-locates with the maximum in eddy kinetic energy ( $EKE$ ;  $EKE = (u'^2 + v'^2 + w'^2)/2$  [ $\text{m}^2/\text{s}^2$ ],  $u', v', w'$  are the residual calculated with respect to the 60-day long model simulation), shown with contours in fig. 3a. The elevated EKE is related to the cascading overflow boluses which dominate the variability of the velocity in the area between the DS sill and the Spill Jet section 300 km downstream (Magaldi *et al.*, 2011; Jochumsen *et al.*, 2012; von Appen *et al.*, 2014b; Voet and Quadfasel, 2010, see also sect. 3.3 of this manuscript). Hereafter, we refer to these bolus-eddy structures collectively as ‘DSO-eddies’ (Denmark Strait Overflow eddies).

We note that the DSO-eddy descent into the Irminger Basin near the convex Dohn Bank radiates internal waves propagating off shore into the Irminger basin (fig. 3b). This indicates that internal waves may be important for the enhanced DSO warming, but if so, their effect will be in time modulated by the passage of the DSO-eddies. We analyze the temporal variability of the DSO mixing and warming in the following section.

### 3.3. Temporal modulation of mixing by the mesoscale variability

We further assess the role of mesoscale variability in DSO mixing by focusing on station 3 (DB) where the transformation rates and the velocity shear are highest. The station time series- and anomaly (residual, as in calculation of  $EKE$ , see above) time series of various variables are shown in fig. 4; only two weeks are shown for clarity. Panel a shows potential density; the dense water boluses are marked by the 27.8-density contour. The density anomaly in the overflow boluses is  $\overline{\Delta\rho^+} \approx 0.1 \text{ kg m}^{-3}$  with respect to the mean and their average vertical extent is  $\overline{d^+} \approx 200$  m. The boluses feature a negative temperature anomaly of 1-2° C (fig. 4b) and peaks in along-flow velocity (fig. 4c), often extending over the entire water column due to the overlying cyclonic eddies (supporting the notion of the ‘DSO-eddies’). Typically, the

270 passage of a DSO-eddy is marked by downwelling as it arrives, then up-  
 271 welling as it departs (fig. 4d), (see Magaldi *et al.*, 2011; Magaldi and Haine,  
 272 2014; Harden *et al.*, 2014, for a more detailed discussion of the eddy-driven  
 273 spilling events). These vertical displacements carrying a negative temper-  
 274 ature anomaly are associated with positive-then-negative enhanced vertical  
 275 eddy temperature flux (VETF) levels (fig. 4e), which points to the role of  
 276 DSO-eddies in local mixing and DSO warming. Note that the relationship  
 277 between the density, velocity and other diagnostics is not obvious during two  
 278 DSO-eddy events captured by fig. 4 (see e.g., day 9 and day 10.5). This is  
 279 due to three-dimensional spatial variability of the flow that is not captured  
 280 by time series in this particular location. In addition, individual DSO-eddy  
 281 events may feature more complicated dynamics when involving intermittent  
 282 spilling of dense water from the shelf (see e.g., fig. 9 in Magaldi *et al.*, 2011)  
 283 and attendant divergence of the velocity field. See Magaldi *et al.* (2011),  
 284 Magaldi and Haine (2014) and Harden *et al.* (2014) for a more detailed dis-  
 285 cussion of the complex three-dimensional flow of the boundary current; here  
 286 we focus on localized influence of the boluses on temperature and mixing  
 287 diagnostics.

288 To further quantify the temporal modulation of mixing and transforma-  
 289 tion by the mesoscale, we calculate time-mean diagnostics conditioned on  
 290 the passage of DSO-eddies (fig. 5). To this end, we extract events of positive  
 291 peak velocity anomalies (DSO-eddy+,  $U \geq \bar{U} + \sigma_U$ ) and periods of slower  
 292 flow (DSO-eddy-,  $U \leq \bar{U} - \sigma_U$ ) for along stream velocity at the depth of  
 293 its peak (average over 650-800 m). The DSO-eddy+ and DSO-eddy- events  
 294 amount to 28% and 34% of the time period, respectively. The results are  
 295 insignificantly different when using other DSO-eddy+ and DSO-eddy- con-  
 296 ditions but the number of time points contributing to the means is smaller  
 297 when the condition is more strict.

298 To quantify the impact of DSO-eddies, we calculate composites of the  
 299 horizontal velocity (fig. 5a). It peaks at the overflow nose (650-800 m) to an  
 300 average of 1.4 m/s during the DSO-eddy+ events, i.e., the flow is twice as  
 301 fast than during the DSO-eddy- periods. The Pearson correlation between  
 302 the along stream velocity at the nose and the velocity shear in the bound-  
 303 ary layer below 800 m is  $r=0.67$  for unfiltered time series, and  $r=0.84$  when  
 304 applying a low-pass Butterworth filter with the cut-off frequency  $1/24 \text{ h}^{-1}$ .  
 305 The scatterplot of the velocity and velocity shear is shown as insert in fig. 5a.  
 306 A clear linear relation between the two quantities motivates future param-  
 307 eterizations. In the bottom boundary layer the stratification is on average

weaker during the DSO-eddy+ events and in 35% of the cases we record a neutral stratification ( $N^2=0$ ). The divergence of the VETF (fig. 5b) leads to a warming of the bottom (densest) waters and a cooling of the interface layer and the ambient water above, and is doubled during the DSO-eddy+ periods with respect to the time mean.

#### 4. Discussion and Conclusions

The sparse observations suggest that mesoscale phenomena and attendant mixing in the Irminger Basin may imprint on the DSO properties (e.g., Voet and Quadfasel, 2010; Falina *et al.*, 2012; Jochumsen *et al.*, 2015; Schaffer *et al.*, 2016) with consequences for the Atlantic Meridional Overturning Circulation (Yeager and Danabasoglu, 2012; Danabasoglu and Coauthors, 2014; Wang *et al.*, 2015).

In this work we employ a high resolution model (2 km horizontal, 15 m in the vertical, 60-day simulation period) to quantify temperature changes and mixing processes in the DSO. We focus on the main overflow pathway along the continental slope in the Irminger Basin (fig. 1a) where the DSO exhibits warming (Voet and Quadfasel, 2010). We study the impact of mesoscale variability on the DSO mixing and water mass property changes in view of motivating future work on sub-grid scale parameterizations in coarse resolution models that would properly represent it. We are focusing on overflow water property changes, vertical mixing diagnostics (vertical shear of horizontal velocity, vertical velocity, vertical eddy heat flux divergence) and mesoscale energy in a 100-km region along the overflow path close to the Denmark Strait. We also quantify time-modulation of these diagnostics by mesoscale variability.

The modeled Lagrangian DSO warming rate (fig. 2c) shows elevated values 100–200 km downstream of the Denmark Strait sill where the DSO warms by about 1 K, which constitutes most of the transformation along the entire 700 km pathway in the Irminger Basin. The model warming rates are consistent with those inferred from measurements (Voet and Quadfasel, 2010) and correspond to the observed net increase in the DSO volume flux from 3 Sv to 5.2 Sv between the Denmark Strait sill and the Spill Jet section (280 km downstream, (Brearley *et al.*, 2012)). The high-resolution model however unravels a strong space-time localization of the warming.

Our model results highlight the role of the mesoscale, namely the DSO boluses and overlying cyclonic eddies. The boluses and cyclones (called here

collectively ‘DSO-eddies’) are prominent flow features in the region where the DSO warming rates are highest downstream from the Denmark Strait sill (between the Dohn Bank and the TTO section) and the velocity shear and the eddy kinetic energy peak throughout the entire water column. The passage of the mesoscale DSO-eddies temporally modulates the time series of temperature and density and diagnostics relevant to mixing (velocity shear, vertical velocity and vertical eddy heat divergence). The DSO-eddies cause increase in the velocity shear and transient unstable stratification in the bottom boundary layer. Notably, our results regarding the mesoscale variability of the DSO are reminiscent of the Faroe Bank Channel Overflow that likewise exhibits a few-day and 20-50 km variability (Seim *et al.*, 2010). Although eddy generation mechanisms and characteristics in the two overflows are different (The Faroe Bank Channel eddies are more baroclinic and are symmetric with respect to the vorticity sign, see Guo *et al.*, 2014), the importance of mesoscale variability is evident in both.

In this work we are not seeking to describe complex three-dimensional dynamics of the boundary current (these were addressed by Magaldi *et al.*, 2011; Magaldi and Haine, 2014) but rather quantify the localized influence of the mesoscale DSO-eddies on temperature and mixing diagnostics in view that these could motivate future parameterization development. The temporal modulation of shear and stratification by the DSO mesoscale variability resolved by our regional model is relevant to the overflow representation in coarse models where routinely the mixing coefficients are functions of the resolved velocity shear and stratification and mesoscale eddies are not resolved. The K-Profile scheme (KPP, Large *et al.*, 1994) used in our model, is employed widely by the ocean modeling community. The KPP is focused on representation of the surface mixing processes. In the interior ocean, it accounts for shear-induced mixing but not for a bottom boundary layer or other effects specific to the overflows. Major improvement of overflow parameterizations emerged from the effort of the Gravity Current Entrainment Climate Process Team (CPT, Legg *et al.*, 2009). They developed a new parameterization (Jackson *et al.*, 2008) that represents the shear-driven entrainment of the ambient water at the top (interfacial) layer of the overflow plume and the mixing within the bottom boundary layer of the plume leading to the homogenization of its properties. Their scheme, implemented in global models with credible results (Wang *et al.*, 2015), accounts for regional differences in turbulent length scales as well as nonlocal turbulent transport but does not include the effects of mesoscale eddies. Recently a new eddy

parameterization has been introduced (Hallberg, 2013) based on eddy length scales and addressing the different model spatial resolutions. However, it does not include the temporal modulation of mixing by mesoscale DSO-eddies nor their intermittent extended impact on velocity, temperature, heat fluxes over the entire water column. These effects need to be addressed by the next generation of parameterizations.

The model results suggest that internal waves may be important in the region of enhanced DSO transformation. DSO-eddy descent into the Irminger Basin near the convex Dohn Bank radiates internal waves evident in both hydrostatic and nonhydrostatic configurations of our model of different resolutions (Magaldi and Haine, 2014). However, the differences in dense water transports are insensitive to the changes in horizontal resolution and vertical momentum dynamics. This can be explained by the limitations of the KPP scheme or by the fact that the waves propagate away into the center of the Irminger Basin with little effect on the slope-bound overflow. The latter explanation is consistent with the distribution of the baroclinic conversion terms and vertical eddy kinetic energy that shows differences between the different configurations only off-shore from the DSO pathway. Future studies with models of higher resolution and not limited by the hydrostatic formulation should assess the role of internal wave processes as well as that of the tides that are excluded in our configuration. The high resolution would also help to elucidate the importance of eddy-topography interaction suggested by observations (Schaffer *et al.*, 2016).

In studying the local modulation of mixing by the mesoscale we focus on vertical mixing diagnostics (the vertical shear of horizontal velocity and the eddy heat divergences) that clearly show time signature of the DSO-eddies. Our results regarding the importance of vertical mixing close to the Denmark Strait to the DSO water property changes are consistent with the conclusions of VQ2010. We choose not to address the mesoscale ‘horizontal stirring’ that is notoriously difficult to quantify by means of horizontal eddy flux statistics. Statistically-significant assessment of horizontal eddy flux divergences requires a long-term (multi-year) time series and a careful choice of the length scale for spatial averaging (see Isachsen *et al.*, 2012, , and references herein). The estimates of ‘horizontal stirring’ by VQ2010 were based on sparse measurements from sections, XBT casts and budget considerations, and these were accompanied by large uncertainties. Trying to reproduce their results with a model and confronting various sources of differences like the sparsity and representativeness of the measurements, interannual variability, and the

model fidelity is beyond the scope of this work. Estimation of the ‘horizontal eddy stirring’ calls for a future collaborative effort using both model and a more recent compilation of existing observations in the Irminger Basin (Paka *et al.*, 2013; von Appen *et al.*, 2014a; Jochumsen *et al.*, 2015; von Appen *et al.*, 2014b) and requires future dedicated measurement campaigns near the Dohn Bank and the TTO section.

In this work, we focused on the main overflow pathway along the continental shelf and excluded the dense water pathways on the East Greenland Shelf that have been hypothesized based on sparse observations (e.g., Rudels *et al.*, 2002; Falina *et al.*, 2012) and investigated in detail by our previous model study (Koszalka *et al.*, 2013, see fig.9). The contribution of shelf pathways to the overflow in terms of the volume flux has been estimated to be only about 1 Sv (Falina *et al.*, 2012). This is likely because the dense water transport onto the shelf is lower than that over the Denmark Strait sill (Macrander *et al.*, 2007) and because the dense water on the shelf is subject to de-densification due to mixing with polar waters (Koszalka *et al.*, 2013). The DSO volume flux along the continental slope in the Irminger Basin is much larger and attendant mixing and entrainment processes likely dominate its variability (3.4 Sv at the Denmark Strait sill doubled by the Angmagssalik section 600 km downstream, Dickson and Brown, 1994; Voet and Quadfasel, 2010). Still, the shelf pathways need further dedicated observational diagnosis and numerical representation in coarse ocean models.

Proper representation of deep overflows in GCMs is crucial for reliable simulations of the present and future climate (Legg *et al.*, 2009; Danabasoglu and Coauthors, 2014; Wang *et al.*, 2015). Our results suggest that the temporal modulation of mixing by the mesoscale variability and the attendant mixing localization should be included in future overflow parameterizations. Targeted field campaigns to further empirically quantify the effect of mesoscale variability on DSO mixing and warming are another high priority.

## 5. Acknowledgments

The authors acknowledge comments and discussions with Anand Gnanadesikan, Victor Zhurbas, Ilker Fer, Detlef Quadfasel, Carsten Eden, Sonya Legg, Kial Stewart, Stephen Jeffress and Alex Fuller. This work was supported in part by NSF grants OCI-108849, OCE-0726640, OCI-0904338 and the Italian Ministry of University and Research through the 348 RITMARE Flagship

455 Project. Data-intensive computations have been performed on the Johns  
456 Hopkins Data-Scope funded by OCI-1040114.

ACCEPTED MANUSCRIPT



## References

- Adcroft, A. and Campin, J.-M. (2004). Rescaled height coordinates for accurate representation of free-surface flows in ocean circulation models. *Ocean Modelling*, **7** (3-4), 269–284.
- Brearley, J. A., Pickart, R. S., Valdimarsson, H., Jonsson, S., Schmitt, R. W., and Haine, T. W. N. (2012). The East Greenland boundary current system south of Denmark Strait. *Deep-Sea Res. I*, **63**, 1–19.
- Bruce, J. G. (1995). Eddies southwest of the Denmark Strait. *Deep-Sea Res. I*, **42**, 13–29.
- Chassignet, E. P. and Coauthors (2009). US GODAE global ocean prediction with the HYbrid Coordinate Ocean Model (HYCOM). *Oceanography*, **22**(2), 64–75.
- Danabasoglu, G. and Coauthors (2014). North Atlantic simulations in Coordinated Ocean-Ice Reference Experiments phase II (CORE-II). part I: Mean states. *Ocean Modelling*, **73**, 76–107.
- Dickson, B., Dye, S., Jonsson, S., Köhl, A., Macrander, A., Marnela, M., Meincke, J., Olsen, S., Rudels, B., Valdimarsson, H., and Voet, G. (2008). The Overflow Flux West of Iceland: Variability, Origins and Forcing. In R. R. Dickson, J. Meincke, and P. Rhines, editors, *Arctic-Subarctic Ocean Fluxes. Defining the Role of the Northern Seas in Climate*, chapter 19, pages 443–474. Springer Science + Business Media, Washington, DC.
- Dickson, R. R. and Brown, J. (1994). The production of North Atlantic Deep Water: Sources, rates and pathways. *J. Geophys. Res.*, **99** (C6), 12319–12341.
- Falina, A., Sarafanov, A., Mercier, H., Lherminier, P., Sokov, A., and Daniault, N. (2012). On the cascading of dense shelf waters in the Irminger Sea. *J. Phys. Ocean.*, **42**, 2254–2267.
- Girton, J. B. and Sanford, T. B. (2003). Descent and modification of the overflow plume in the Denmark Strait. *J. Phys. Ocean.*, **33**, 1351–1364.
- Girton, J. B., Sanford, T. B., and Käse, R. H. (2001). Synoptic sections of the Denmark Strait Overflow. *Geophys. Res. Lett.*, **28**(8), 1619–1622.
- Guo, C., Ilicak, M., Fer, I., Darelius, E., and Bentsen, M. (2014). Baroclinic instability of the Faroe Bank Channel overflow. *J. Phys. Ocean.*, **44**, 2698–2717.

- 489 Guo, C., Ilicak, M., Bentsen, M., and Fer, I. (2016). Characteristics of the Nordic  
490 Seas overflows in a set of Norwegian Earth System Model experiments. *Ocean*  
491 *Modelling*, **104**, 112–128.
- 492 Hallberg, R. (2013). Using a resolution function to regulate parameterizations of  
493 oceanic mesoscale eddy effects. *Ocean Modelling*, **72**, 92–103.
- 494 Harden, B. E., Pickart, R. S., and Renfrew, I. A. (2014). Offshore transport of  
495 dense water from the East Greenland Shelf. *J. Phys. Ocean.*, **44**, 229–245.
- 496 Hill, A. E. (1996). Spin-down and the dynamics of dense pool gyres in shallow  
497 seas. *J. Mar. Res.*, **54**(3), 471–486.
- 498 Isachsen, P. E., Koszalka, I., and LaCasce, J. H. (2012). Observed and modelled  
499 surface eddy heat fluxes in the eastern Nordic Seas. *J. Geophys. Res.*, **117**,  
500 C08020.
- 501 Jackson, L., Hallberg, R., and Legg, S. (2008). A parameterization of shear-driven  
502 turbulence for ocean climate models. *J. Phys. Ocean.*, **38**, 1033–1053.
- 503 Jochumsen, K., Quadfasel, D., Valdimarsson, H., and Jónsson, S. (2012). Vari-  
504 ability of the Denmark Strait Overflow: Moored time series from 1996–2011. *J.*  
505 *Geophys. Res.*, **117**, C12003.
- 506 Jochumsen, K., Kollner, M., Quadfasel, D., Dye, S., Rudels, B., and Valdimarsson,  
507 H. (2015). On the origin and propagation of Denmark Strait Overflow Water  
508 anomalies in the Irminger Basin. *J. Geophys. Res.*, **120**, 1841–1855.
- 509 Jungclauss, J. H., Macrandar, A., and Käse, R. H. (2008). Modelling the Over-  
510 flows across the Greenland–Scotland Ridge. In R. R. Dickson, J. Meincke,  
511 and P. Rhines, editors, *Arctic–Subarctic Ocean Fluxes. Defining the Role of*  
512 *the Northern Seas in Climate*, chapter 22, pages 527–549. Springer Science +  
513 Business Media, Washington, DC.
- 514 Kalnay, E. and Coauthors (1996). The NCEP/NCAR 40-Year Reanalysis Project.  
515 *Bull. Amer. Meteor. Soc.*, **77**, 437471.
- 516 Käse, R. H. and Oschlies, A. (2000). Flow through Denmark Strait. *J. Geophys.*  
517 *Res.*, **105**(C12), 28257–28546.
- 518 Käse, R. H., Girton, J. B., and Sanford, T. B. (2003). Structure and variability of  
519 the Denmark Strait Overflow: Model and observations. *J. Geophys. Res.*, **108**,  
520 3181.

- 521 Köhl, A., Käse, R. H., Stammer, D., and Serra, N. (2007). Causes of changes in  
522 the Denmark Strait Overflow. *J. Phys. Ocean.*, **37**, 1678–1696.
- 523 Koszalka, I. M., Haine, T. W. N., and Magaldi, M. G. (2013). Fates and travel times  
524 of Denmark Strait Overflow Water in the Irminger Basin. *J. Phys. Oceanogr.*,  
525 **43**(12), 2611–2628.
- 526 Large, W. G., McWilliams, J. C., and Doney, S. C. (1994). Oceanic vertical mixing:  
527 A review and a model with a nonlocal boundary layer parametrization. *Rev.*  
528 *Geophys.*, **32**, 363–403.
- 529 Legg, S., Ezer, T., Jackson, L., Briegleb, B., Danabasoglu, G., Large, W., Wu,  
530 W., Chang, Y., Ozgokmen, T. M., Peters, H., Xu, X., Chassignet, E. P., Gor-  
531 don, A. L., Griffies, S., Hallberg, R., Price, J., Riemenschneider, U., and Yang,  
532 J. (2009). Improving oceanic overflow representation in climate models: The  
533 gravity current entrainment Climate Process Team. *Bull. Amer. Meteor. Soc.*,  
534 **90**, 657–670.
- 535 Macrander, A., Send, U., Valdimarsson, H., Jónsson, S., and Käse, R. H. (2005).  
536 Interannual changes in the overflow from the Nordic Seas into the Atlantic Ocean  
537 through Denmark Strait. *Geophys. Res. Lett.*, **32**, L06606.
- 538 Macrander, A., Käse, R. H., Send, U., Valdimarsson, H., and Jónsson, S. (2007).  
539 Spatial and temporal structure of the Denmark Strait Overflow revealed by  
540 acoustic observations. *Ocean. Dyn.*, **57**, 75–89.
- 541 Magaldi, M. G. and Haine, T. W. N. (2014). Hydrostatic and non-hydrostatic  
542 simulations of dense waters cascading off a shelf: the East Greenland case.  
543 *Deep-Sea Res. I.*
- 544 Magaldi, M. G., Haine, T. W. N., and Pickart, R. S. (2011). On the nature and  
545 variability of the East Greenland Spill Jet: a case study in summer 2003. *J.*  
546 *Phys. Oceanogr.*, **41**(12), 2307–2327.
- 547 Paka, V., Zhurbas, V., Rudels, B., Quadfasel, D., Korzh, A., and Delisi, D. (2013).  
548 Microstructure measurements and estimates of entrainment in the Denmark  
549 Strait Overflow plume. *Ocean Sci.*, **9**, 1003–1014.
- 550 Pickart, R. S., Torres, D. J., and Frantantoni, P. S. (2005). The East Greenland  
551 Spill Jet. *J. Phys. Ocean.*, **35**, 1037.
- 552 Rudels, B., Fahrbach, E., Meincke, J., Budeus, G., and Eriksson, P. (2002). The  
553 East Greenland Current and its contribution to the Denmark Strait overflow.  
554 *ICES J. Mar. Sci.*, **219**, 319–325.

- 555 Rudels, B., Eriksson, P., Buch, E., Budeus, G., and Fahrbach, E. (2003). Temporal  
556 switching between sources of the Denmark Strait overflow water. *ICES J. Mar.*  
557 *Sci.*, **59**, 1133–1154.
- 558 Schaffer, J., Kanzow, T., Jochumsen, K., Lackschewitz, K., Tippenhauer, S.,  
559 Zhurbas, V. M., and Quadfasel, D. (2016). Enhanced turbulence driven by  
560 mesoscale motions and flow-topography interaction in the Denmark Strait Over-  
561 flow plume. *J. Geophys. Res. Oceans*, **121**, 7650–7672.
- 562 Seim, K. S., Fer, I., and Berntsen, J. (2010). Regional simulations of the Faroe  
563 Bank Channel overflow using a  $\sigma$ -coordinate ocean model. *Ocean Modelling*,  
564 **35**, 31–44.
- 565 Serra, N., Käse, R., and D. Stammer, A. K., and Quadfasel, D. (2010). On the  
566 low-frequency phase relation between the Denmark Strait and the Faroe Bank  
567 Channel overflows. *Tellus*, **62**(4), 530–550.
- 568 Voet, G. and Quadfasel, D. (2010). Entrainment in the Denmark Strait Overflow  
569 plume by meso-scale eddies. *Ocean Sci.*, **6**, 301–310.
- 570 von Appen, W.-J., Koszalka, I. M., Pickart, R. S., Haine, T. W. N., Mastopole,  
571 D., and Magaldi, M. G. (2014a). East Greenland Spill Jet as important part of  
572 the AMOC. *Deep-Sea Res. I*, **92**, 75–84.
- 573 von Appen, W.-J., Pickart, R. S., Brink, K. H., and Haine, T. W. N. (2014b). Wa-  
574 ter column structure and statistics of Denmark Strait Overflow Water cyclones.  
575 *Deep-Sea Res. I*, **84**, 110–126.
- 576 Wang, H., Legg, S., and Hallberg, R. W. (2015). Representations of the Nordic  
577 Seas overflows and their large scale climate impact in Coupled Models. *Ocean*  
578 *Modelling*, **86**, 76–92.
- 579 Whitehead, J. A. (1998). Topographic control of oceanic flows in deep passages  
580 and straits. *Rev. Geophys.*, **36**, 423–440.
- 581 Yeager, S. and Danabasoglu, G. (2012). Sensitivity of Atlantic Meridional Circu-  
582 lation variability to parametrized Nordic Seas overflows in CCSM. *J. Climate*,  
583 **25**, 2077–2103.
- 584 Zhang, H.-M., Bates, J. J., and Reynolds, R. W. (2006). Assessment of composite  
585 global sampling: Sea surface wind speed. *Geophys. Res. Lett.*, **33**, L17714.

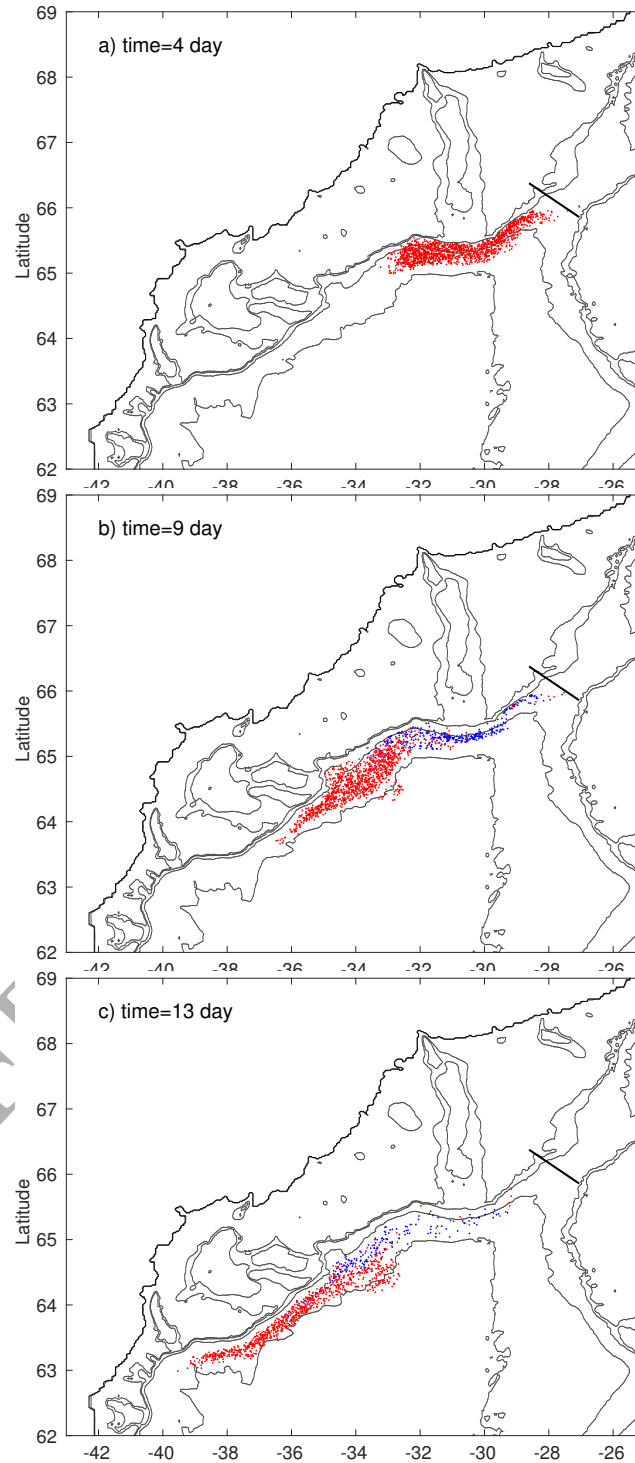


Figure 1: A sequence of ensemble particle positions projected on the horizontal plane on days: 4 (a), 9 (b), 13 (c). The particles were released every half a day over 5 days but time is counted individually for each particle since its release. Particles originating at the Denmark Strait sill are marked in red, those released on the adjacent shelf in blue. The coastline and bathymetric contours of 350, 450, 1000 and 2000 m are shown.

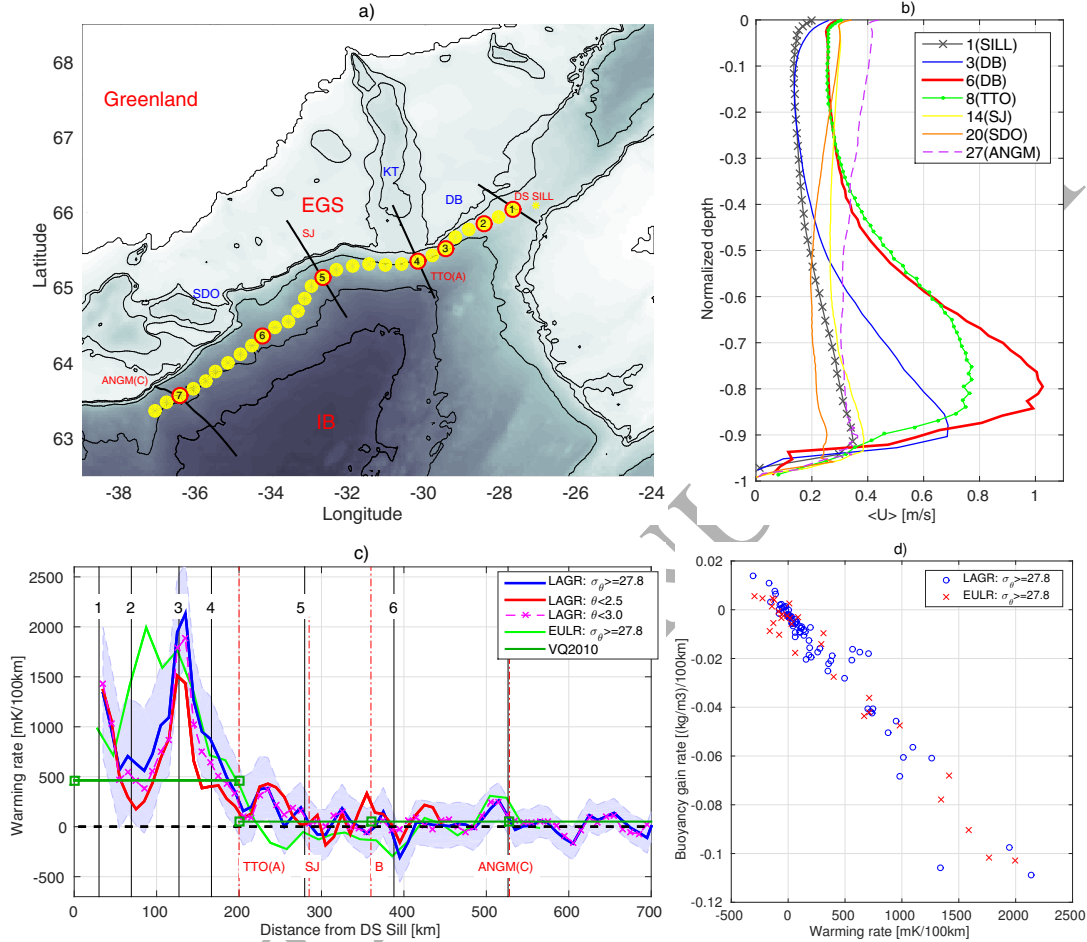


Figure 2: a) A part of the model domain showing the Irminger Basin (IB) and the East Greenland Shelf (EGS) with stations along the DSO path (yellow dots, selected stations have red circles). The hydrographic sections (black lines) are: Denmark Strait, TTO, Spill Jet (SJ) and Angmagssalik (ANGM). Denmark Strait sill (DS sill), Kangerdlugssuaq Trough (KT), Dohrn Bank (DB) and Sermilik Deep Opening (SDO) are marked. The coastline and bathymetric contours of 350, 450, 1000, 2000 and 2500 m are shown. The intensity of gray shading scales with depth of the water column. b) Normalized (with respect to local depth), time-mean profiles of along-stream speed  $U$  at selected sections. c) Warming rates derived from dense particles (LAGR) binned in 20-km distance bins following the DSO path for different DSO definitions used by VQ2010; their warming rate estimates (from standard sections A–C) are shown with dark green straight lines. The Eulerian estimate along the same path (EULR) is shown in light green. The confidence intervals are from the standard deviation of the binned particle temperatures for the (LAGR:  $\sigma \geq 27.8$ ) particle set. d) Scatterplot of the mean warming- and buoyancy gain rates along the DSO path (panel a) from Lagrangian (LAGR) and Eulerian (EULR) estimates.

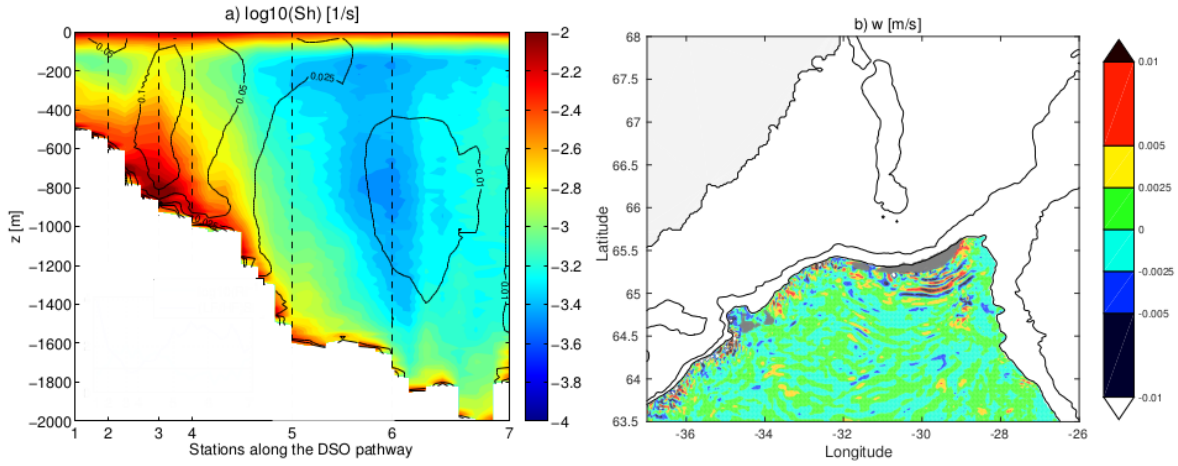


Figure 3: (a) Time-averaged vertical shear of horizontal velocity along the DSO pathway shown in Fig. 1a. Superimposed are contours of constant total eddy kinetic energy ( $[m^2/s^2]$ ). (b) A snapshot of the vertical velocity field ( $[m/s]$ ) at 1000 m depth during a passage of a beddy ( $\sigma_\theta \geq 27.8$  at 1000 m depth patched in gray) triggering internal waves near the Dohrn Bank.

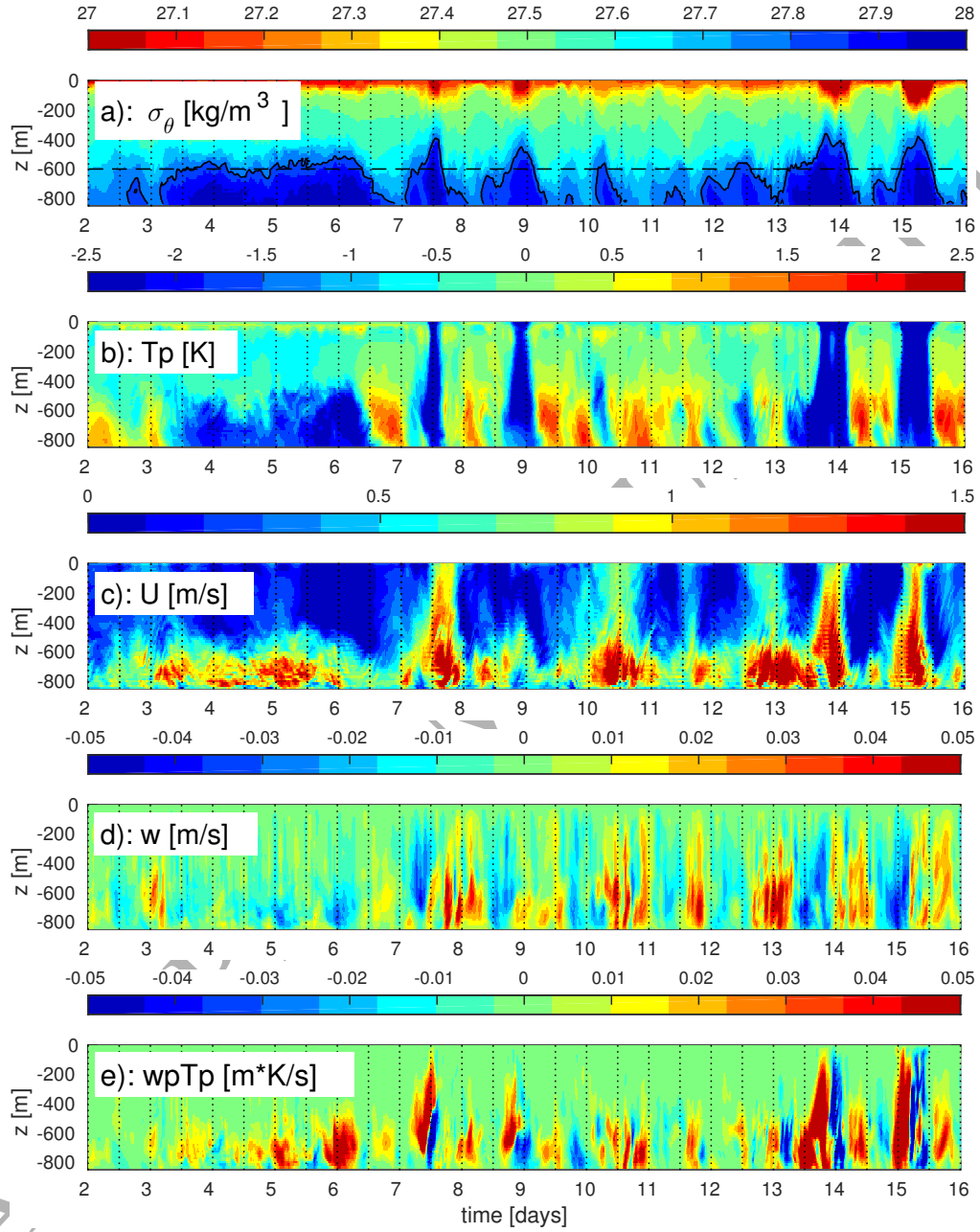


Figure 4: Time series at Station 3 (DB) of: (a) potential density, with the 27.8-isopycnal marked with a black line. (b) temperature anomaly, (c) along-stream velocity, (d) vertical velocity, (e) product of vertical velocity- and temperature anomaly. The anomalies are calculated with respect to the two-month long simulation but only two weeks are shown for clarity.



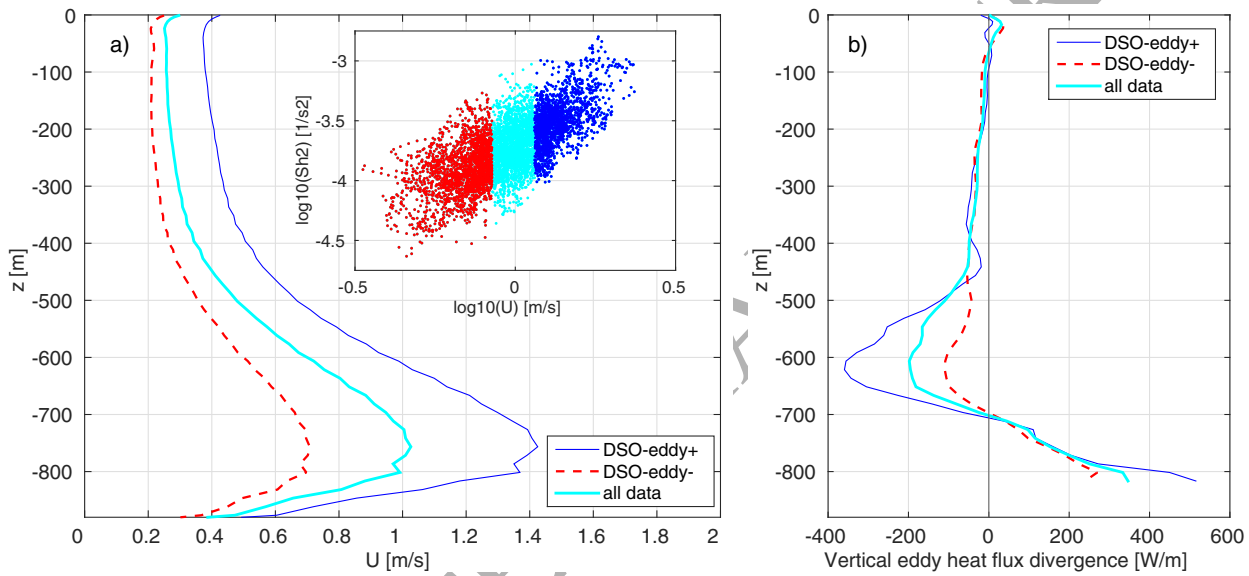


Figure 5: Time-average profiles at Station 3 (DB) for all data and conditioned on the presence of mesoscale Denmark Strait eddies ('DSO-eddies', see text), of: (a) along-stream velocity. The insert scatterplot shows timeseries of squared shear  $Sh^2$  at the bottom boundary layer (below 800 m) versus along-stream velocity at 650–800 m (depth of the peak velocity), (b) vertical eddy heat flux divergence.